Changes in Widespread Aquifer Properties caused by a Magnitude 6 Class Earthquake evaluated using InSAR Analyses

Yutaro Shigemitsu[1], Kazuya Ishitsuka[1], and Weiren Lin[2]

[1]Kyoto University
[2]Graduate School of Engineering, Kyoto University

November 22, 2022

Abstract

The correlation between surface displacements and groundwater level changes has been widely used to understand aquifer properties and their site characteristics; however, the underlying mechanism of various correlation types and influence of earthquakes has not been fully investigated. In this study, we examine correlations in Osaka and Kyoto, Japan, over 4 years including the period of the June 18, 2018, Mw 5.6 northern Osaka earthquake surface displacement from InSAR analyses and groundwater level monitoring data. Both positive and negative correlations were identified at groundwater level observation stations. Based on the different types of correlations, we propose a new conceptual aquifer model that drives the opposite interaction between the surface displacement and the groundwater level change. We further reveal that sites with negative correlations increased after the earthquake, suggesting that the earthquake increased the groundwater recharge rate as a result of increases in aquifer transportation properties such as permeability and porosity.

Hosted file

essoar.10511747.1.docx available at https://authorea.com/users/536391/articles/599053-changes-in-widespread-aquifer-properties-caused-by-a-magnitude-6-class-earthquake-evaluated-using-insar-analyses

Yutaro Shigemitsu[1], Kazuya Ishitsuka[1], and Weiren Lin[1]

[1]Department of Urban Management, Graduate School of Engineering, Kyoto University, Kyoto, Japan.

Corresponding author: Yutaro Shigemitsu (shigemitsu.yutaro.76u@st.kyoto-u.ac.jp)

Key Points:

- Surface displacement and groundwater level change were mapped with high spatial density before and after the 2018 northern Osaka earthquake
- We propose a new model of aquifer connectivity on the basis of positive and negative correlations between the displacement and the change
- Mw 6 class earthquakes could change aquifer properties over a wide area, causing enhancements in negative seasonal correlations

Abstract

The correlation between surface displacements and groundwater level changes has been widely used to understand aquifer properties and their site characteristics; however, the underlying mechanism of various correlation types and influence of earthquakes has not been fully investigated. In this study, we examine correlations in Osaka and Kyoto, Japan, over 4 years including the period of the June 18, 2018, Mw 5.6 northern Osaka earthquake surface displacement from InSAR analyses and groundwater level monitoring data. Both positive and negative correlations were identified at groundwater level observation stations. Based on the different types of correlations, we propose a new conceptual aquifer model that drives the opposite interaction between the surface displacement and the groundwater level change. We further reveal that sites with negative correlations increased after the earthquake, suggesting that the earthquake increased the groundwater recharge rate as a result of increases in aquifer transportation properties such as permeability and porosity.

Plain Language Summary

Groundwater level changes cause changes in the pore water pressure and water load, which in turn cause surface displacements. Recently, the correlation between the surface displacement and groundwater level changes has been revealed using Interferometric Synthetic Aperture Radar (InSAR) analyses, a technique capable of widely estimating surface displacements. However, the mechanism of the correlation is still not clear. In this study, we estimate the surface displacements during a period including the Mw 5.6 northern Osaka earthquake that occurred on June 18, 2018, in Osaka and Kyoto, Japan, and examine its correlation with the groundwater level changes. We find that positive and negative correlations were scattered at each groundwater level observation site, indicating that the aquifer system is complicated and changing even over short ranges. In addition, the negative correlations became larger after the earthquake. This might be due to the increase in the recharge rate, resulting from the increase in the porosity and infiltration rate caused by the earthquake.

1 Introduction

Natural hazards, such as earthquakes, droughts, floods, and typhoons, pose risks to the conservation and management of groundwater resources. In particular, earthquakes cause widespread crustal deformation, altering the crustal properties and impacting the quantity and level of the groundwater. Crustal deformation data over a wide area and in time series play an important role in examining the area and progression of earthquake impacts.

Interferometric Synthetic Aperture Radar (InSAR) is a rapidly advancing geodetic observation technique used to obtain wide-area, time-series surface displacement data. InSAR analyses have spread to a variety of fields, following its initial application to the surface deformation induced by the 1992 Landers earthquake (Massonnet et al., 1993; Wald and Heaton, 1994; Fialko et al., 2004). Recently, it has been applied to the estimation of surface displacements caused by hydraulic head changes, and many previous studies have revealed permeability, land use types, or storage coefficients related to correlations between hydraulic head changes and surface displacements (Chaussard et al., 2014b; Normand et al., 2015; Malinowska et al., 2020; Zhou et al., 2020). Surface displacements that result from groundwater level changes are also induced by earthquakes (King et al., 2006; Ishitsuka et al., 2017; Liu et al., 2018; Ishitsuka et al., 2020). Furthermore, recent studies have shown that surface displacements that have resulted from hydraulic head changes prior to an earthquake may serve as earthquake precursors, reflecting the subtle alteration of the crustal permeability depending on the crustal stress state (Moro et al., 2017; Wang et al., 2019). Because appropriate groundwater monitoring requires an intensive understanding of the overall interactions between groundwater and aquifer skeletons, understanding the mechanisms of such correlations, the impact of earthquakes on these correlations, and the relationship between earthquakes and aquifer properties is essential.

Seasonal surface displacements caused by seasonal hydraulic head changes have attracted attention with respect to understanding the site characteristics of aquifers over wide areas (Demoulin, 2006; Demoulin et al., 2007); such characteristics include the spatial distribution of the skeletal storage coefficient (Bell et al., 2008; Chaussard et al., 2014a; Chen et al., 2017; Hu et al., 2018; Mourad et al., 2021) and the aquifer connectivity (Ishitsuka et al., 2014; Chaussard et al., 2014a; Neely et al., 2021). Most previous studies regarded the correlation between the seasonal surface displacement and the hydraulic head change as a positive relationship (i.e., ground uplift with increasing groundwater level and vice versa). A positive correlation can be explained by the change in the pore pressure according to the change in the hydraulic head. However, a recent study by Lu et al. (2020) demonstrated that the correlation can be negative (i.e., ground uplift/subsidence in response to decreasing/increasing groundwater level). In their conceptual model, negative correlations were explained by the cumulative water mass load because an increasing load (i.e., an increase in the hydraulic head) can lead to subsidence (Panda et al., 2018; Zhan et al., 2021; Heki et al., 2022). The conceptual model implies that whether the correlation is positive or negative could depend on the balances between the influences of the pore pressure and the water mass load (Lu et al., 2020). We speculate that such a variety of groundwater-induced displacement mechanisms may have occurred in many aquifer systems worldwide. However, only a few examples of studies discuss these positive and negative correlations. Moreover, understanding the mechanisms and site characteristics of such contrary types of correlations is crucial to interpreting InSAR surface displacement data.

Accordingly, this study quantifies the correlation between groundwater level changes and surface displacements using data at 21 groundwater level observation sites from January 2017 to December 2020, including the 2018 northern Osaka Mw 5.6 earthquake that occurred throughout the Osaka Plain and Kyoto Basin in Japan. Using an InSAR analysis and a dense groundwater observation network, we show a variety of correlation types in the aquifer system and update the existing conceptual model to explain these positive and negative correlations. On the basis of the analysis, we explain the impact of the Mw 5.6 northern Osaka earthquake that occurred on June 18, 2018 (Hirata et al. 2018), by showing changes in the parameters related to the permeability and elastic properties. To the best of our knowledge, this is the first study to find that Mw 6 class earthquakes, which occur frequently worldwide, can change crustal properties over wide areas and can change the seasonal correlation between the surface displacement and groundwater level changes. We believe this finding can contribute to understanding of the prerequisite knowledge required for groundwater monitoring.

2 Data and Methods

The InSAR analysis was performed using data obtained from Sentinel-1, a European Space Agency satellite, to estimate surface displacements. A total of 102 scenes acquired from December 24, 2016, to December 27, 2020, were used in the ascending orbit and 102 scenes acquired from December 30, 2016, to December 21, 2020, were used in the descending orbit to investigate the effects of the 2018 northern Osaka earthquake on the surface displacements (Figure 1a; see also Table S1).

Groundwater level data from January 1, 2017, to December 31, 2020, at 21 groundwater level observation sites published by the Water Quality Database were used (Ministry of Land, Infrastructure, Transport and Tourism, Japan, 2021). One-hourly groundwater level data were sampled to convert to a daily average. The 21 groundwater level observation sites located near the epicenter of the northern Osaka earthquake were selected (Figure 1b; see also Table S2). Of these, 15 observation sites are above unconfined aquifers and 6 sites are above confined aquifers (see Table S2). The depth intervals of the strainers at all the wells were shallower than 70 m (see Table S2).

In this study, we used a persistent scatterer InSAR (PSInSAR) analysis, which can extract only stable pixels with little noise (Kampes, 2006; see also Text S1). A PSInSAR analysis usually assumes a linear constant-velocity model of the surface displacement (Ferretti et al., 2000; Ferretti et al., 2001); accordingly, this study also follows this assumption. However, linearity may not be maintained because of the occurrence of the earthquake. Therefore, we prepared the primary data in two periods, before and after the earthquake, and separated the InSAR analysis into these two periods (Figure 1a). In this paper, results under the conditions of an amplitude dispersion index of adx = 0.25 and a phase coherence of coh = 0.60 are treated as representative results. PS pixels are often located at manmade objects in urban areas; therefore, the analysis is suitable for surface displacement estimations in the Osaka Plain and the Kyoto Basin, where major cities (Osaka and Kyoto) are located. This target area contains abundant underground aquifers (Taniguchi et al., 2005), and the correlation between the surface displacements and the groundwater level changes has been qualitatively pointed out in the past (Hashimoto et al., 2016). When comparing the obtained surface displacements with changes in the groundwater levels, PS pixels within a 1-km square around each groundwater observation station site were extracted and the average surface displacement value of these PS points was used for comparison with the groundwater level. Furthermore, for comparison with the groundwater levels, we performed a 2.5-dimensional analysis to calculate the surface displacement in the vertical direction using data from southward and northward orbits (Fujiwara et al., 2000; see also Text S2).

$$R_{\mathrm{xy}}(\tau) = \frac{\overline{x(t)y(t+\tau)}}{\sqrt{\overline{x^2}\bullet\overline{y^2}}}\#(1)$$

Because we calculated the CCCs each year, six correlation coefficients for each condition between January 2017 and December 2020 were obtained at each site. We then calculated the averages and standard deviations of the coefficients for each site.

3 Results

3.1 Characteristics of the surface displacements and groundwater level changes

We found that the annual displacement patterns revealed by the Sentinel-1 interferograms differed before and after the earthquake (Figure 2a and 2b; see also Figure S1). The uplift in the black framed area in Figure 2a and 2b agrees with the results of other InSAR analyses (Morishita, 2021), and our results further show that the areas of uplift became even larger after the earthquake. Comparing the annual groundwater level changes before and after the earthquake, the map patterns of the annual surface displacement after the earthquake (Figure 2b) are generally correlated with the groundwater level changes (Figure S2). This agreement of the patterns likely indicates that the uplift and subsidence after the northern Osaka earthquake are associated with groundwater level changes. In fact, even if a location is not near a ruptured fault, earthquakes can cause changes in the groundwater level and pore water pressure via permeability modification, which results in the elastic expansion/contraction of the aquifer (e.g., Moro et al., 2017; Wang et al., 2019). However, we found that the annual displacement pattern before the earthquake showed only a weak correlation with the groundwater level change (Figures 2a and S2).

Comparing the time-series surface displacements and groundwater level changes, we found seasonal correlations at 18 groundwater level observation sites (Figures 2c–2f and S3). We classified the patterns of the seasonal correlations into three categories: positive correlation (PC), negative correlation (NC), and no correlation (UC). Sites H and N were categorized as PC, showing the ground surface rising and subsiding in correspondence with the groundwater level increases and decreases, respectively (Figure 2c and 2d). The UC category was identified at three sites, C, D, and T, where the time-series surface displacements were not significantly related to the groundwater level changes (Figure S3). The other 16 sites belong to the NC category. In these NC sites, we found that the time-series surface displacements and groundwater level changes were negatively correlated. The surface subsides despite increases in the groundwater level, and the surface rises when the groundwater level falls (Figure 2e and 2f). The groundwater level changes at the NC sites are linked to seasonal changes in precipitation (see Figure S4), whereas the groundwater level changes at the PC sites may be linked to temporal groundwater extraction. Focusing on the negative correlations, we found that the negative correlations became more significant after the 2018 northern Osaka earthquake because of the larger surface displacements. For example, at sites Q and C, the negative correlations between the time-series surface displacements and the groundwater level changes were not significant prior to the earthquake; however, the correlations became more significant after the earthquake (Figure 2e and 2f).

The time-series surface displacements and groundwater levels at each observation site are shown in Figure S3. Seasonal correlations are observed around all the groundwater level sites, except for the UC sites, C, D, and T. The peaks in the correlations, including both positive and negative correlations, appear approximately every 365 days (see Figure S5). Even though some previous studies have pointed out that the correlation between the time-series displacement and the groundwater level may have a time lag (Normand et al., 2015; Zhou et al., 2020), the time-series data used in this study did not exhibit significant time lags.

3.2 Quantification of the correlations between the time-series displacement and the groundwater level

The results of the coefficients for the entire analyzed period are shown in Figure 3a (see also Table S3). The CCC patterns were generally consistent with the qualitative classifications of PC, NC, and UC described in Section 3.1. Because the orders of the standard deviations were mostly smaller than those of the average, we concluded that the variations in the coefficients for each year were not large and that the CCC site differences were statistically significant.

3.3 Correlation changes before and after the 2018 northern Osaka earthquake

We calculated the change in the CCCs before and after the 2018 northern Osaka earthquake (Figure 3b; see also Table S4) by dividing the surface displacement and groundwater level change data into two periods (Figure 1a). The standard deviations did not change significantly before and after the earthquake. One of the main findings of this study is that the CCCs are clearly visible as being smaller for all sites except one. In other words, the CCCs shifted from PC before the earthquake to NC after the earthquake. Furthermore, some of the observations, where no correlation was observed before the earthquake, also showed an increase in negative correlations after the earthquake. It is difficult to assume that any event other than the earthquake caused the change in the correlation during that period; therefore, we interpret the changes in the correlation as being induced by the 2018 northern Osaka earthquake. To the best of our knowledge, such changes in the correlation before and after earthquakes have not been previously reported.

To examine the spatial characteristics of the correlation change, we plotted the distribution of the changes in the correlation at each site (Figure 3c and 3d). The spatial pattern at the groundwater level observation sites shows that the type of correlation change was different even over short distances. The spatial pattern implies that the aquifer characteristics are spatially complex and that aquifer properties may be highly heterogeneous. For example, site H shows positive correlation and site G shows negative correlation. Compared with a previous study by Lu et al. (2020), our calculation showed that the correlations between the surface displacements and the groundwater level changes were more spatially dense, therefore demonstrating the effectiveness of InSAR analyses and dense groundwater measurements to classify the characteristics of aquifers at a higher resolution.

4 Discussion

4.1 Possible aquifer models

Lu et al. (2020) proposed that seasonal surface displacements depend on the balance between the pore pressure and the water mass load in an aquifer. We checked whether the aquifers at each site being confined or unconfined was an influential factor determining the type of correlation (i.e., positive or negative); however, this proved irrelevant. This indicates that the conceptual model does not depend on whether the aquifer is unconfined or confined.

Positive correlations were observed at two sites, N and H, where groundwater is extracted from deep underground; the groundwater level changes in shallow aquifers correlate with groundwater pumping from depth (Figure 2e and 2f). This indicates that the deep groundwater level change is linked with the shallow groundwater level changes in these sites. On the basis of this interpretation, we propose a new conceptual aquifer model (Figure S6). In the area where the surface displacement is positively correlated with the hydraulic head, a shallow aquifer may be connected to a deep aquifer that is in contact with a deep impermeable layer. Because of the vertical connectivity, we assume that the effect of the water mass load is mitigated by the impermeable layer, while the effect of the pore water pressure increases. Conversely, at sites showing negative correlation, the observed aquifer is not assumed to be connected to a deep aquifer; therefore, the effect of the water mass load is larger, for example, subsidence occurs because of the mass load of the surface water. At the UC sites, especially sites C, D, and T, there was no seasonal component to the groundwater level changes, suggesting that they reflect complex aquifer structures.

4.2 Change in the groundwater response and aquifer properties before and after the earthquake

To investigate whether the groundwater level response to precipitation changed, we applied a numerical equation (Park et al., 2008) to the daily average groundwater level data at the groundwater level observation site Q in Ayukawa and the daily average precipitation data at the precipitation observation site in Ibaraki (Figure 1b). $h = h_0\ \exp\left(\mathrm{kt}\right) + \frac{\alpha P(exp(\mathrm{kt})-1)}{\mathrm{kn}}\#(2)$

Here, h, P, and t indicate the groundwater level, precipitation obtained at discrete intervals, and time, respectively, and $k,\ \alpha$, and n are the rate coefficient to groundwater discharge, the ratio of recharge to precipitation, and the fillable porosity in the ground, respectively. h, P, and t are observations, and we estimated $\frac{\alpha}{n}$ and k (see also Text S4).

The estimated value of the groundwater level is in good agreement with the maximum peak value of the measured value, especially prior to the earthquake, suggesting a good representation of the increase in the groundwater level as a result of precipitation during the examined period (Figure 4a). Conversely, the measured values frequently exceeded the estimated values after the earthquake (Figure 4a). This result suggests that the amount of groundwater per unit of precipitation increased as a result of the earthquake, for example, the permeability may have increased as a result of the earthquake, as suggested in previous studies (King et al., 2006; Liu et al., 2018). Note that the estimated minimum peak does not agree with the measured values. This mismatch occurs because Eq. (2) does not consider the drainage from the initial value (Figure 4a).

The estimated parameters in Eq. (2) were $\frac{\alpha}{n} = 1.5 \times 10^{-3}$ and $k = -5.9 \times 10^{-2}$ T^{-1} before the earthquake and $\frac{\alpha}{n} = 1.5 \times 10^{-3}$ and $k = -2.7 \times 10^{-2}$ T^{-1} after the earthquake. Because k is proportional to the inverse of n, this implies that n and became twice as large after the earthquake. This result suggests that the earthquake increased the porosity and recharge rate of the groundwater and therefore increased the amount of groundwater, as proposed in Elkhoury et al. (2006) and Manga et al. (2012). Our observation and interpretation support our hypothesis that the negative correlations were enhanced by the earthquake because the negative correlation appears when the pore water pressure becomes large (Elkhoury et al., 2006; Manga et al., 2012).

4.3 Change in the pseudoelastic constant before and after the earthquake

The enhancement of the negative correlation between the surface displacements and the groundwater level changes also implies that the susceptibility of the surface displacements per unit change in the hydraulic head was likely altered by the earthquake. To investigate this phenomenon in more detail, we calculated the ratio of the daily groundwater level changes to the daily surface displacements and compared the ratios before and after the earthquake. When the groundwater level changes and surface displacements are positively correlated, their ratio is known as the skeletal storage coefficient (Chen et al., 2017; Ishitsuka et al., 2019). However, this does not hold when the correlation is negative. Instead, we treat the constant ratio as a pseudoelastic constant because a negative correlation indicates that the surface displacements were caused primarily by the water mass load according to Lu et al. (2020). A positive value of the pseudoelastic constant indicates that the surface displacements were caused primarily by the pore water pressure, while a negative value indicates that the surface displacements were caused primarily by the water mass load. The absolute value of the pseudoelastic constant indicates the degree of susceptibility to surface displacements caused by groundwater level changes (see also Text S5).

The calculated pseudoelastic constant at the groundwater level observation site Q is shown in Figure 4b. At this site, the pseudoelastic constant was negative, suggesting that the ground displacements were caused by the water mass load. The estimated pseudoelastic constants before and after the earthquake at all observation sites are shown in Figure 4c. At most sites, the pseudoelastic constants became smaller after the earthquake, for example at Ayukawa (see Figure S7). The exception is site N, Yahataminami, where the pseudoelastic constant was positive and the pseudoelastic constant became larger after the earthquake. This increase in the constant is likely due to the increase in the pore water pressure as opposed to the increase in the water mass load. The increase in the absolute value of the pseudoelastic constant suggests that the seismic-induced increase in the permeability and porosity (Elkhoury et al., 2006; Manga et al., 2012) resulted in a modification of the elastic properties of the aquifer.

5 Conclusions

In this study, by applying a PSInSAR analysis to the Osaka and Kyoto areas, Japan, where the 2018 northern Osaka earthquake occurred, we found that Mw 6 class earthquakes can influence aquifer property changes over a wide area. This finding was based on the conceptual aquifer model of Lu et al. (2020) and our results using CCCs showing that seasonal surface displacements were correlated with groundwater level changes. To the best of our knowledge, this is the first time that it has been confirmed that Mw 6 class earthquakes affect not only the linear correlation between surface displacements and groundwater level changes but also the seasonal negative correlation. The change in the correlation is explained by changes in the aquifer properties (i.e., porosity, permeability, and the recharge rate of the ground) induced by the earthquake. This is the first time that satellite data have been used to determine changes in aquifer properties over a wide area after an earthquake. In other words, we have captured a new important natural phenomenon of long-term seasonal changes caused by earthquakes. The results were validated from multiple perspectives, including possible aquifer models, pre- and post-earthquake groundwater responses, aquifer properties, quasi-elastic constants, and changes in the spatial properties. Explanations of the overall mechanisms of surface displacements after earthquakes will contribute to obtaining useful information for groundwater level monitoring and subsurface resource development.

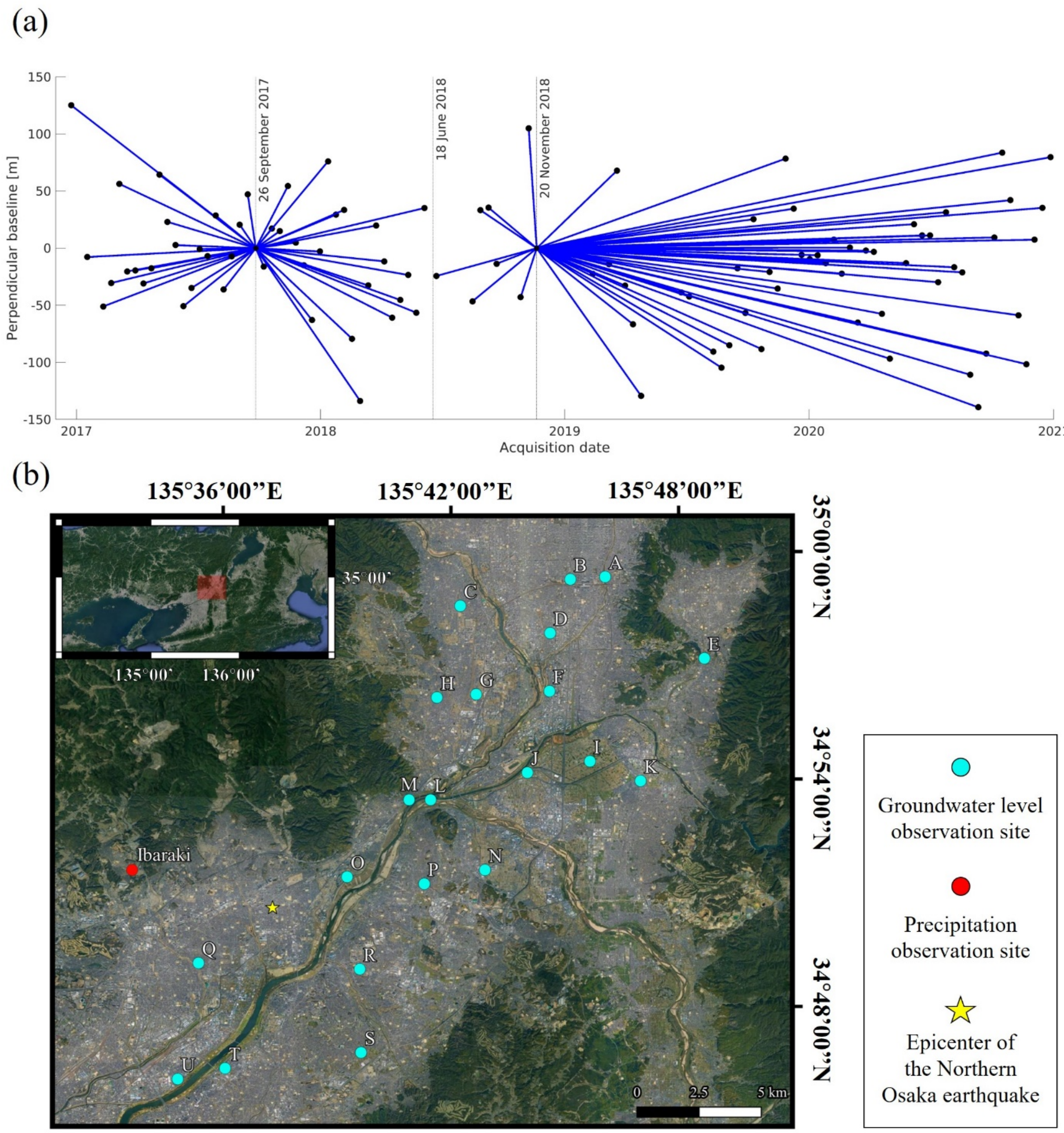

Fi

1. (a) Combination of Sentinel-1 data used for InSAR analysis. The vertical axis shows the perpendicular baseline, and the horizontal axis shows the date of the radar irradiations by the satellite in the descending orbit. Data obtained in September 26, 2017 and November 20, 2018, respectively were used as reference

data for InSAR analysis bordering on June 18, 2018 when the northern Osaka earthquake occurred. (b) The study area including the Osaka Plain and the Kyoto Basin. The inset shows the area of middle Japan. The groundwater level observation sites are sorted by alphabet from A to U (see Table S2). The background data are hosted by Environmental Systems Research Institute, Inc.

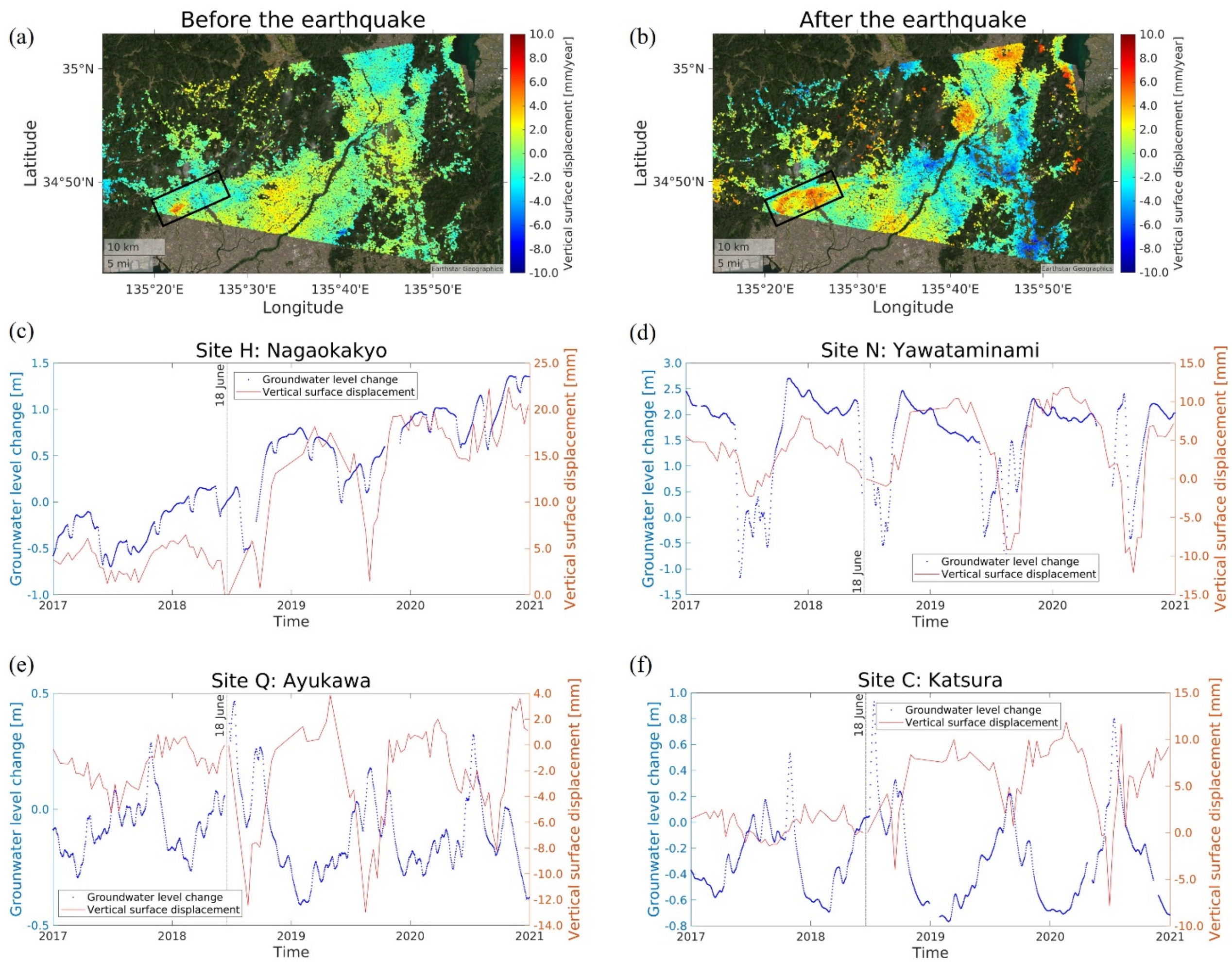

Figure 2. Annual surface displacements by PSInSAR analysis of (a) before the earthquake and (b) after the earthquake. Blue indicates subsidence displacement, red indicates uplift and black star indicates the epicenter of the earthquake. (c), (d), (e), (f) Comparison of time-series of surface displacements and groundwater level changes at sites H, N, Q and C.

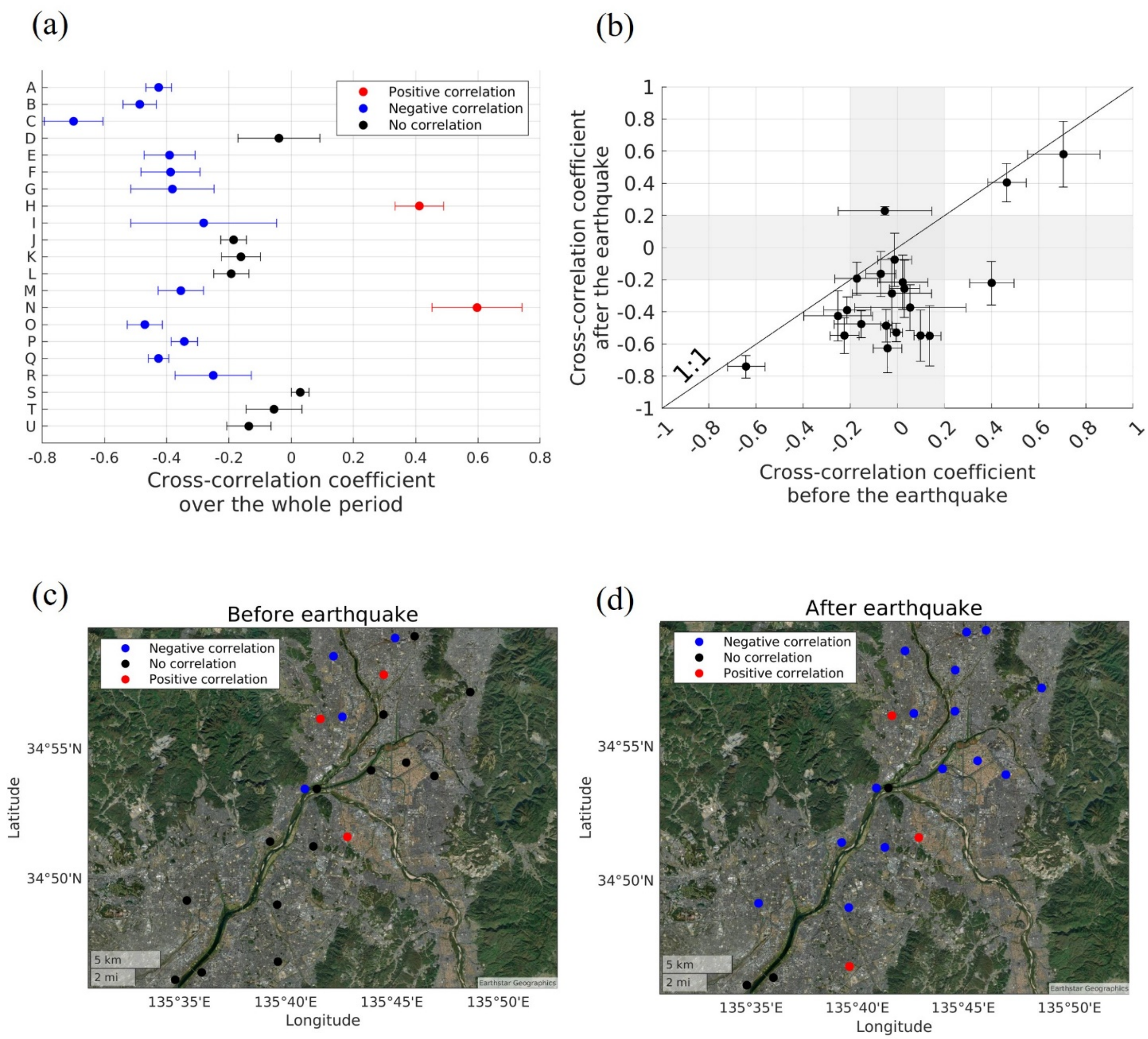

Figure 3. (a) Comparison of cross-correlation coefficients (CCCs) between surface displacements and groundwater level changes from 2017 to 2020. The time lag to calculate the coefficient was set to zero days. The solid circles and er-

ror bars indicate the average and standard deviations of CCCs between surface displacements obtained from the six conditions of PSInSAR analysis and groundwater level changes, respectively. (b) Comparison of the CCCs before and after the 2018 northern Osaka earthquake. The straight line indicates 1 : 1. (c), (d) Distribution of CCCs before (c) and after (d) the earthquake for all the groundwater level observation sites in the Osaka and Kyoto area (see Table S2 for the symbols).

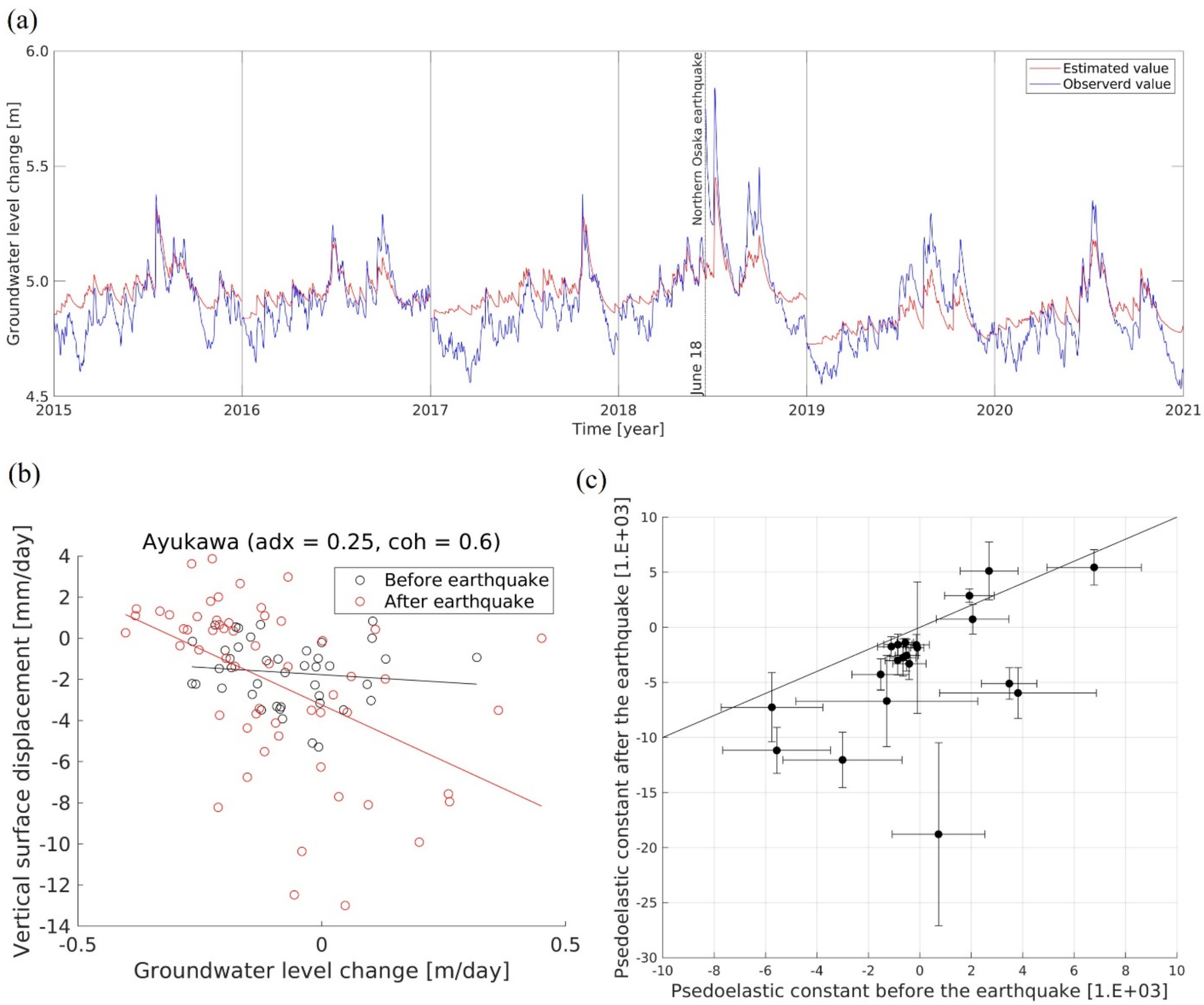

Figure 4. Investigations of crustal property changes due to the earthquake. (a) Comparison of estimated groundwater level change by the numerical algorithm

(Park et al., 2008) and observed groundwater level change. (b) Change of pseudoelastic constants before and after the earthquake at site Q: Ayukawa. The slope of the straight line is the inverse of the pseudoelastic constant. (c) Variation of pseudoelastic constants before and after the earthquake. The straight line represents 1 : 1. The black circles and error bars indicate the average values and the standard deviations.

Acknowledgments

We would like to express our gratitude to the European Space Agency (ESA) for providing the Sentinel-1 data, and the Water Quality Database of the Ministry of Land, Infrastructure, Transport and Tourism (MLIT), Japan for providing the groundwater level and observation sites data in accordance with their open data policy. We also would like to thank the Japanese Meteorological Agency for providing precipitation data. We thank Martha Evonuk, PhD, from Edanz (https://jp.edanz.com/ac) for editing a draft of this manuscript.

Open Research

Data Availability Statement

The authors would like to thank the European Space Agency (ESA) (https://search.asf.alaska.edu/#/), and the Water information System, Ministry of Land, Infrastructure, Transport and Tourism (http://www1.river.go.jp/). The SLC data for InSAR analysis and groundwater level data are available through https://zenodo.org/record/6644133#.YrVRrnbP2Uk

(DOI: https://doi.org/10.5281/zenodo.6644133). The .dat file contains data on groundwater level changes. Groundwater level data is hourly, and each line contains data for one day (24 hours). The name of the .dat files consists of the name of the groundwater level station and the observation period. Datasets that include raw in the name contain the respective date in the first column. SLC data for InSAR analysis can be obtained by running the .py files in python. Python files are provided to obtain SLC data by two orbits, Ascending and Descending, respectively.

References

Bell, J. W., Amelung, F., Ferretti, A., Bianchi, M., & Novali, F. (2008). Permanent scatterer InSAR reveals seasonal and long-term aquifer-system response to groundwater pumping and artificial recharge. *Water Resources Research*, *44*, W02407. https://doi.org/10.1029/2007WR00152

Chaussard, E., Burgmann, R., Shirzaei, M., Fielding E. J., & Baker, B. (2014a). Predictability of hydraulic head changes and characterization of aquifer-system and fault properties from InSAR-derived ground deformation. *J. Geophys. Res.*, *119*, 6572-6590. https://doi.org/10.1002/2014JB011266

Chaussard, E., Wdowinski, S., Cabral-Cano, E., & Amelung, F. (2014b). Land subsidence in central Mexico detected by ALOS InSAR time-series. *Remote Sensing of Environment*, *140*, 94–106. https://doi.org/10.1016/j.rse.2013.08.038

Chen, J., Knight, R., & Zebker, H. A. (2017). The temporal and spatial variability of the confined aquifer head and storage properties in the San Luis Valley, Colorado inferred from multiple InSAR mission. Water Resources Research, 53, 9708-9720. https://doi.org/10.1002/2017WR20881

Demoulin, A. (2006). Slip rate and mode of the Feldbiss normal fault (Roer Valley Graben) after removal of groundwater effects. *Earth and Planetary Science Letters*, *245*(3), 630–641. https://doi.org/10.1016/j.epsl.2006.03.030

Demoulin, A., Ducarme, B., & Everaerts, M. (2007). Seasonal height change influence in GPS and gravimetric campaign data. *Journal of Geodynamics*, *43*, 308. https://doi.org/10.1016/j.jog.2006.09.008

Elkhoury, J. E., Brodsky, E. E., & Agnew, D. C. (2006). Seismic waves increase permeability. *Nature*, *441*(7097), 1135–1138. https://doi.org/10.1038/nature04798

Ferretti, A., Prati, C., & Rocca, F. (2000). Nonlinear subsidence rate estimation using permanent scatterers in differential SAR interferometry. *IEEE Transactions on Geoscience and Remote Sensing: A Publication of the IEEE Geoscience and Remote Sensing Society*, *38*(5), 2202–2212. https://doi.org/10.1109/36.868878

Ferretti, A., Prati, C., & Rocca, F. (2001). Permanent scatterers in SAR interferometry. *IEEE Transactions on Geoscience and Remote Sensing: A Publication of the IEEE Geoscience and Remote Sensing Society*, *39*(1), 8–20. https://doi.org/10.1109/36.898661

Fialko, Y. (2004). Evidence of fluid-filled upper crust from observations of postseismic deformation due to the 1992Mw7.3 Landers earthquake. *Journal of Geophysical Research*, *109*(B8). https://doi.org/10.1029/2004jb002985

Fujiwara, S., Nishimura, T., Murakami, M., Nakagawa, H., Tobita, M., & Rosen, P. A. (2000). 2.5-D surface deformation of M6.1 earthquake near Mt Iwate detected by SAR interferometry. *Geophysical Research Letters*, *27*(14), 2049–2052. https://doi.org/10.1029/1999gl011291

Hashimoto, M. (2016). Observation of ground deformation in the Osaka and Kanto plains with ALOS-2/PALSAR-2. *2016 IEEE International Geoscience and Remote Sensing Symposium (IGARSS)*, 3855–3858. https://doi.org/10.1109/IGARSS.2016.7730000

Heki, K., & Arief, S. (2022). Crustal response to heavy rains in Southwest Japan 2017-2020. *Earth and Planetary Science Letters*, *578*(117325), 117325. https://doi.org/10.1016/j.epsl.2021.117325

Hirata, N., & Kimura, R. (2018). The Earthquake in Ōsaka-Fu Hokubu on 18 June 2018 and its Ensuing Disaster. *Journal of Disaster Research*, *13*(4), 813–816. https://doi.org/10.20965/jdr.2018.p0813

Hooper, A., Bekaert, D., Spaans, K., & Arıkan, M. (2012). Recent advances in SAR interferometry time series analysis for measuring crustal deformation. *Tectonophysics*, *514-517*, 1–13. https://doi.org/10.1016/j.tecto.2011.10.013

Hooper, A., & Zebker, H. A. (2007). Phase unwrapping in three dimensions with application to InSAR time series. *Journal of the Optical Society of America. A, Optics, Image Science, and Vision*, *24*(9), 2737–2747. https://doi.org/10.1364/josaa.24.002737

Hu, W., Lu, Z., & Wang, T. (2018). Characterization of hydrogeological properties in Salt Lake Valley, Utah, using InSAR. *J. Geophys. Res.*, *123*, 1257-1271. https://doi.org/10.1029/2017JF004497

Ishitsuka, K., Fukushima, Y., Tsuji, T., Yamada, Y., Matsuoka, T., & Giao, P. H. (2014). Natural surface rebound of the Bangkok plain and aquifer characterization by persistent scatterer interferometry. *Geochem. Geophys. Geosys.*, *15(4)*, 965-974. https://doi.org/10.1002/2013GC005154

Ishitsuka, K., Matsuoka, T., Nishimura, T., Tsuji, T., & ElGharbawi, T. (2017). Ground uplift related to permeability enhancement following the 2011 Tohoku earthquake in the Kanto Plain, Japan. *Earth Planets Space*, *69*:81. https://doi.org/10.1186/s40623-017-0666-7

Ishitsuka, K., & Tsuji, T. (2019). Mapping Surface Displacements and Aquifer Characteristics Around the Kumamoto Plain, Japan, Using Persistent Scatterer Interferometry. IGARSS 2019 - 2019 IEEE International Geoscience and Remote Sensing Symposium, 9654–9657. https://doi.org/10.1109/IGARSS.2019.8897893

Ishitsuka, K., Tsuji, T., Lin, W., Kagabu, M., & Shimada, J. (2020). Seasonal and transient surface displacements in the Kumaoto area, Japan, associated with the 2016 Kumamoto earthquake: implications for seismic-induced groundwater level change. *Earth Planets Space*, *72*:144. https://doi.org/10.1186/s40623-020-01275-2

Kampes, B. M. (2006). Radar Interferometry. Springer Netherlands. https://doi.org/10.1007/978-1-4020-4723-7

King, C.-Y., Zhang, W., & Zhang, Z. (2006). Earthquake-induced Groundwater and Gas Changes. *Pure and Applied Geophysics*, *163*(4), 633–645. https://doi.org/10.1007/s00024-006-0049-7

Liu, C.-Y., Chia, Y., Chuang, P.-Y., Chiu, Y.-C., & Tseng, T.-L. (2018). Impacts of hydrogeological characteristics on groundwater-level changes induced by earthquakes. *Hydrogeology Journal*, *26*(2), 451–465. https://doi.org/10.1007/s10040-017-1684-z

Lu, C.-Y., Hu, J.-C., Chan, Y.-C., Su, Y.-F., & Chang, C.-H. (2020). The Relationship between Surface Displacement and Groundwater Level Change and Its Hydrogeological Implications in an Alluvial Fan: Case Study of the Choshui River, Taiwan. *Remote Sensing*, *12*(20), 3315. https://doi.org/10.3390/rs12203315

Malinowska, A. A., Witkowski, W. T., Guzy, A., & Hejmanowski, R. (2020). Satellite-based monitoring and modeling of ground movements caused by water rebound. *Remote Sensing*, *12*(11), 1786. https://doi.org/10.3390/rs12111786

Manga, M., Beresnev, I., Brodsky, E. E., Elkhoury, J. E., Elsworth, D., Ingebritsen, S. E., Mays, D. C., & Wang, C.-Y. (2012). Changes in permeability caused by transient stresses: Field observations, experiments, and mechanisms. *Reviews of Geophysics*, *50*(2). https://doi.org/10.1029/2011rg000382

Ministry of Land, Infrastructure, Transport and Tourism, Japan. (2021). Water information System, Ministry of Land, Infrastructure, Transport and Tourism, Japan,2017-2020 [Dataset]. http://www1.river.go.jp/

Morishita, Y. (2021). Nationwide urban ground deformation monitoring in Japan using Sentinel-1 LiCSAR products and LiCSBAS. *Progress in Earth and Planetary Science*, *8*(1), 6. https://doi.org/10.1186/s40645-020-00402-7

Moro, M., Saroli, M., Stramondo, S., Bignami, C., Albano, M., Falcucci, E., Gori, S., Doglioni, C., Polcari, M., Tallini, M., Macerola, L., Novali, F., Costantini, M., Malvarosa, F., & Wegmüller, U. (2017). New insights into earthquake precursors from InSAR. *Scientific Reports*, *7*(1), 12035. https://doi.org/10.1038/s41598-017-12058-3

Massonnet, D., Rossi, M., Carmona, C., Adragna, F., Peltzer, G., Feigl, K., & Rabaute, T. (1993). The displacement field of the Landers earthquake mapped by radar interferometry, *Nature*, *364*, 138-142. https://doi.org/10.1038/364138a0

Mourad, M., Tsuji, T., Ikeda, T., Ishitsuka, K., Senna, S., & Ide, K. (2021). Mapping aquifer storage properties using S-wave velocity and InSAR-derived surface displacement in the Kumamoto area, southwest Japan. *Remote Sensing*, *13(21)*, 4391. https://doi.org/10.3390/rs13214391

Neely, W. R., Borsa, A. A., Burney, J. A., Levy, M. C., Silverii, F., & Sneed, M. (2021). Characterization of groundwater recharge and flow in California's San Joaquin valley from InSAR-observed surface deformation. *Water Resources Research*, *57*, e2020WR028451. https://doi.org/10.1029/2020WR028451

Normand, J. C. L., & Heggy, E. (2015). InSAR Assessment of Surface Deformations in Urban Coastal Terrains Associated With Groundwater Dynamics. *IEEE Transactions on Geoscience and Remote Sensing: A Publication of the IEEE Geoscience and Remote Sensing Society*, *53*(12), 6356–6371. https://doi.org/10.1109/TGRS.2015.2437368

Panda, D., Kundu, B., Gahalaut, V. K., Bürgmann, R., Jha, B., Asaithambi, R., Yadav, R. K., Vissa, N. K., & Bansal, A. K. (2018). Seasonal modulation of deep slow-slip and earthquakes on the Main Himalayan Thrust. *Nature Communications*, *9*(1), 1–8. https://doi.org/10.1038/s41467-018-06371-2

Park, E., & Parker, J. C. (2008). A simple model for water table fluctuations in response to precipitation. *Journal of Hydrology*, *356*(3-4), 344–349. https://doi.org/10.1016/j.jhydrol.2008.04.022

Taniguchi, M., & Uemura, T. (2005). Effects of urbanization and groundwater flow on the subsurface temperature in Osaka, Japan. *Physics of the Earth and Planetary Interiors*, *152*(4), 305–313. https://doi.org/10.1016/j.pepi.2005.04.006

Wald, D. J., & Heaton, T. H. (1994). Spatial and temporal distribution of slip for the 1992 Landers, California, earthquake. *Bulletin of the Seismological Society of America*, *84*(3), 668–691. https://doi.org/10.1785/BSSA0840030668

Wang, S., Xu, W., Xu, C., Yin, Z., Bürgmann, R., Liu, L., & Jiang, G. (2019). Changes in groundwater level possibly encourage shallow earthquakes in central Australia: The 2016 Petermann

ranges earthquake. *Geophysical Research Letters*, *46*(6), 3189–3198. https://doi.org/10.1029/2018gl080510
Werner, C., Wegnüller, U., Strozzi, T., & Wiesmann, A. (2000). Gamma SAR and interferometric processing software. *Proc. ERS-ENVISAT Symp: European Space Agency Special Publication*, *461*.

Wegnüller, U., Werner, C., Strozzi, T., Wiesmann, A., Frey, O., & Santoro, M. (2016). Sentinel-1 support in the GAMMA software. *Procedia Computer Science*, *100*, 1305–1312. https://doi.org/10.1016/j.procs.2016.09.246

Zhan, W., Heki, K., Arief, S., & Yoshida, M. (2021). Topographic amplification of crustal subsidence by the rainwater load of the 2019 typhoon hagibis in japan. *Journal of Geophysical Research, [Solid Earth]*, *126*(6). https://doi.org/10.1029/2021jb021845

Zhou, C., Gong, H., Chen, B., Gao, M., Cao, Q., Cao, J., Duan, L., Zuo, J., & Shi, M. (2020). Land Subsidence Response to Different Land Use Types and Water Resource Utilization in Beijing-Tianjin-Hebei, China. *Remote Sensing*, *12*(3), 457. https://doi.org/10.3390/rs12030457

Geophysical Research Letters

Supporting Information for

Changes in Widespread Aquifer Properties caused by a Magnitude 6 Class Earthquake evaluated uing InSAR Analyses

Yutaro Shigemitsu[1], Kazuya Ishitsuka[1], and Weiren Lin[1]

[1]Department of Urban Management, Graduate School of Engineering, Kyoto University, Kyoto, Japan.

Contents of this file

Text S1 to S5
Figures S1 to S7
Tables S1 to S4

Introduction

Text S1 describes the conditions under which PSInSAR analysis was performed.

Text S2 describes 2.5-dimensional analysis.

Text S3 describes methods for calculating cross-correlation coefficients and preprocessing of the data to be used.

Text S4 describes the numerical equation using the daily average groundwater level data and the daily average precipitation data.

Text S5 describes the specific definition of pseudoelastic constant.

Text S1.

Gamma software was used for differential interferometric processing (Werner et al., 2000; Wegmüller et al., 2016). Stamps, developed by Stanford University, was used for phase unwrapping (Hooper et al., 2007; Hooper et al., 2012). To remove atmospheric noise, we performed a temporal filtering (Ferretti et al., 2000) with a moving average of 200 × 200 pixels in the spatial direction and 30 days in the temporal direction. We changed the parameters in the PSC selection and PS selection sections to obtain results for a total of six analysis conditions, as shown in the following equations.

$$\boldsymbol{\hat{\sigma}_{\phi} = \frac{\sigma_a}{\bar{a}}} \tag{1'}$$

$$\boldsymbol{\Gamma = \frac{1}{N}\left|\sum_{n=1}^{N} exp\{j(\phi_{noise})\}\right|} \tag{2'}$$

where $\boldsymbol{\sigma_a}$ is the standard variance of the amplitude and $\boldsymbol{\bar{a}}$ is the average of the amplitude of a pixel. $\boldsymbol{\phi_{noise}}$ denotes the stochastic observation error due to the decrease in coherence. $\boldsymbol{n}$ and $\boldsymbol{N}$ denote the number of interferometric pairs and the total number of interferometric pairs, respectively. The amplitude dispersion index ($\boldsymbol{adx}$, $\boldsymbol{\hat{\sigma}_{\phi}}$) was tested for two conditions, $\mathbf{0.25}$ and $\mathbf{0.35}$, and the phase coherence ($\boldsymbol{coh}$, $\boldsymbol{\Gamma}$) was tested for three conditions, $\mathbf{0.60}$, $\mathbf{0.70}$ and $\mathbf{0.80}$. The annual displacements were then calculated from the estimated time-series displacements using the least squares method under each condition. The geobasemap satellite in MATLAB was used as the background for the mapping.

Text S2.

Specifically, a plane along the two vectors of the satellite line of sight for the northward and southward orbits was obtained, and the vertical and east-west displacements in that plane were calculated using the following equation.

$$\boldsymbol{D_{LOS}} = [-\cos\boldsymbol{\alpha}\sin\boldsymbol{\theta} \quad \sin\boldsymbol{\alpha}\sin\boldsymbol{\theta} \quad \cos\boldsymbol{\theta}][\boldsymbol{D_{EW}} \quad \boldsymbol{D_{NS}} \quad \boldsymbol{D_{UD}}]^{\mathbf{T}} \qquad (\mathbf{3'})$$

where $\boldsymbol{D_{LOS}}$ represents the displacement in the satellite line-of-sight direction, and $\boldsymbol{D_{EW}}$, $\boldsymbol{D_{NS}}$, and $\boldsymbol{D_{UD}}$ represent the displacement in the east-west, north-south, and up-down directions, respectively. $\boldsymbol{\theta}$ is the angle of incidence, and $\boldsymbol{\alpha}$ is the directional angle of the satellite flight with respect to clock-wise direction with north direction as positive. However, the dates of the data obtained from the northward and southward orbits differed by approximately six days. For this reason, the vertical displacements obtained were adjusted to the date of the data obtained from the southward orbit.

Text S3.

$$\boldsymbol{R_{xy}(\tau) = \overline{x(t)y(t+\tau)} \Big/ \sqrt{\overline{x^2} \cdot \overline{y^2}}} \qquad (\mathbf{1})$$

where $\boldsymbol{R_{xy}}$ is the CCC ($\boldsymbol{-1 \leq R_{xy} \leq 1}$), $\boldsymbol{\bar{x}}$ is the average groundwater level change, $\bar{\mathbf{y}}$ is the average vertical surface displacement, $\boldsymbol{t}$ is time, and $\boldsymbol{\tau}$ is time shift. In this study, positive correlations were considered for $\boldsymbol{R_{xy}}$ values larger than 0.2, negative correlations for $\boldsymbol{R_{xy}}$ values smaller than -0.2 and no correlations otherwise.

Before calculating the CCC, we applied a pre-processing which reduce the linear component. In the first period, we used June 11, 2018 as the reference date, and in the second period, June 23, 2018 as the reference date (on the reference date, surface displacement was zero). The data were resampled by spline interpolation to obtain the same number of samples as the groundwater level changes data, and the 10-day moving average was calculated. The data were normalized by the absolute values of the maximum and minimum values when the maximum and minimum values exceeded 1 mm and -1 mm, respectively. The linear trend representing the long-term trend was then removed in order to evaluate the seasonal correlations. Similarly, the data of groundwater level change was also processed. The missing data were resampled by spline interpolation, with June 18, 2018 as the reference date, and then the linear trend indicating the long-term trend was removed. High-frequency variations in groundwater level changes were observed at four sites D, F, P and T, so the high-frequency changes were removed by applying a 14-day moving average process. Finally, the data were normalized by the absolute values of the maximum and minimum values when the maximum and minimum values exceeded 1 m and -1 m, respectively.

Text S4.

The groundwater level data ($\boldsymbol{h}$) and precipitation data ($\boldsymbol{P}$) for one year before the earthquake in 2016 were used to determine $\boldsymbol{\alpha}$ / $\boldsymbol{n}$ and $\boldsymbol{k}$. These data were then used to calculate the estimated groundwater level for each year from 2015 to 2020 (Figure 4a). The groundwater level on January 1 of each year was used as the initial value for the calculation. The fmincon algorithm in MATLAB was used to solve the nonlinear optimization problem.

Text S5.

When the pseudoelastic constant becomes small, a slight increase in pore water pressure or water mass load will cause surface displacements. In this study, we estimated the pseudoelastic constants by dividing the surface displacements and groundwater level changes data into before and after the earthquake. Specifically, the least-squares method was applied to each data before and after the earthquake to obtain the slope of the line that shows the inverse of the pseudoelastic constant.

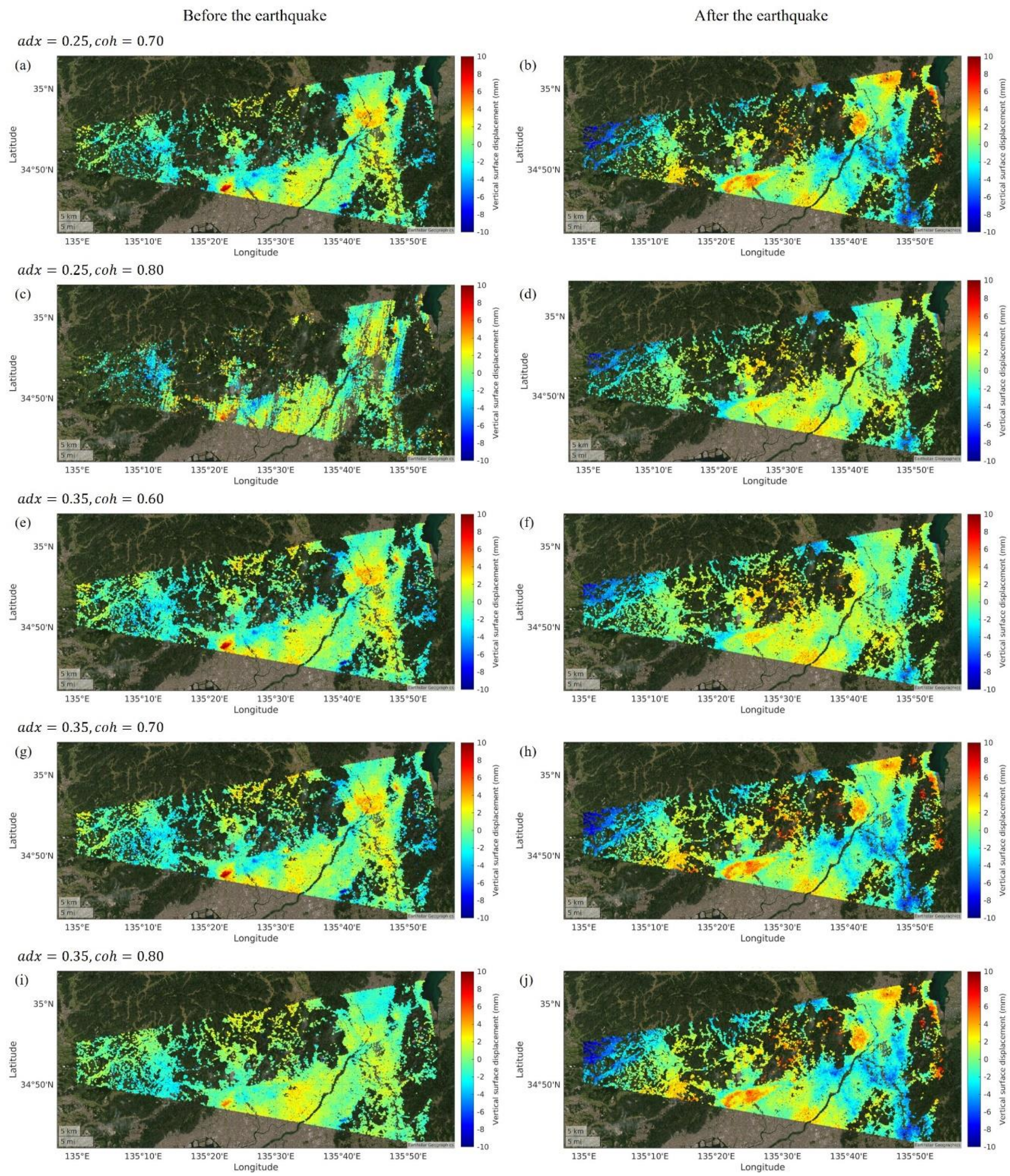

Figure S1. Annual surface displacements of the target area in the vertical direction for all conditions other than $\boldsymbol{adx = 0.25}$, $\boldsymbol{coh = 0.60}$.

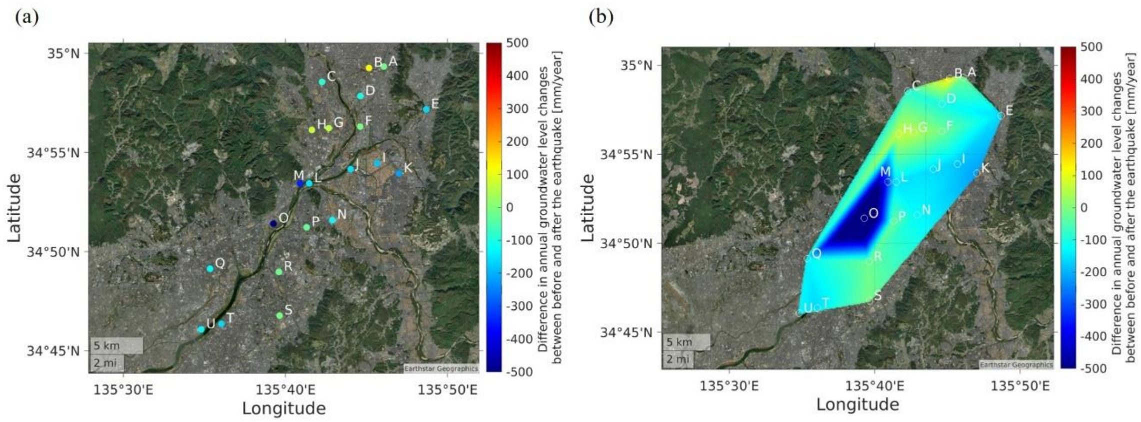

Figure S2. (a) Difference in annual groundwater level changes between before and after the earthquake at each groundwater level observation site. (b) The two-dimensional linear interpolation based on triangulation was applied to (a).

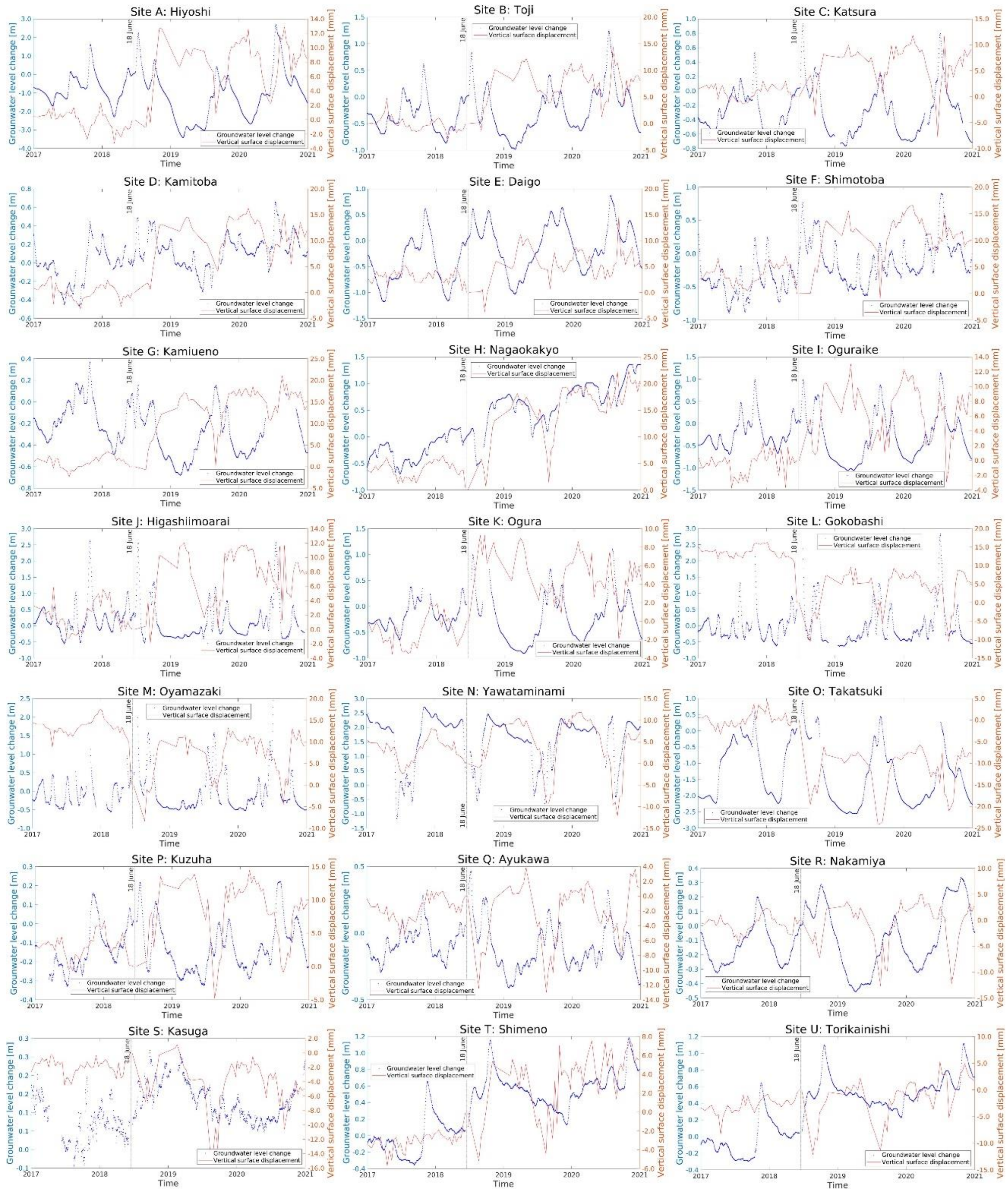

Figure S3. Comparison of surface displacements and groundwater level changes at each groundwater level observation site when $\boldsymbol{adx} = \mathbf{0.25}$ and $\boldsymbol{coh} = \mathbf{0.60}$.

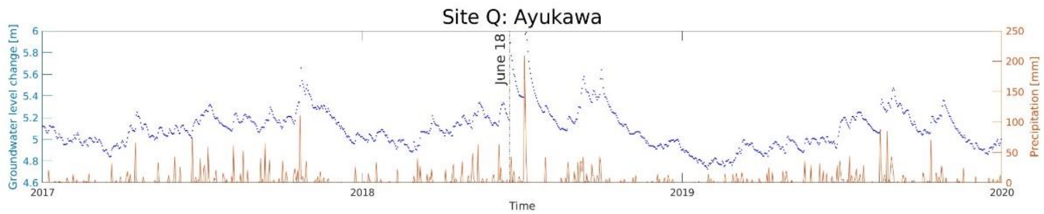

Figure S4. The example of seasonal groundwater level change depends on the amount of precipitation. As an example, we compared the groundwater level change at the groundwater level observation site Ayukawa with the precipitation at the precipitation observation site Ibaraki.

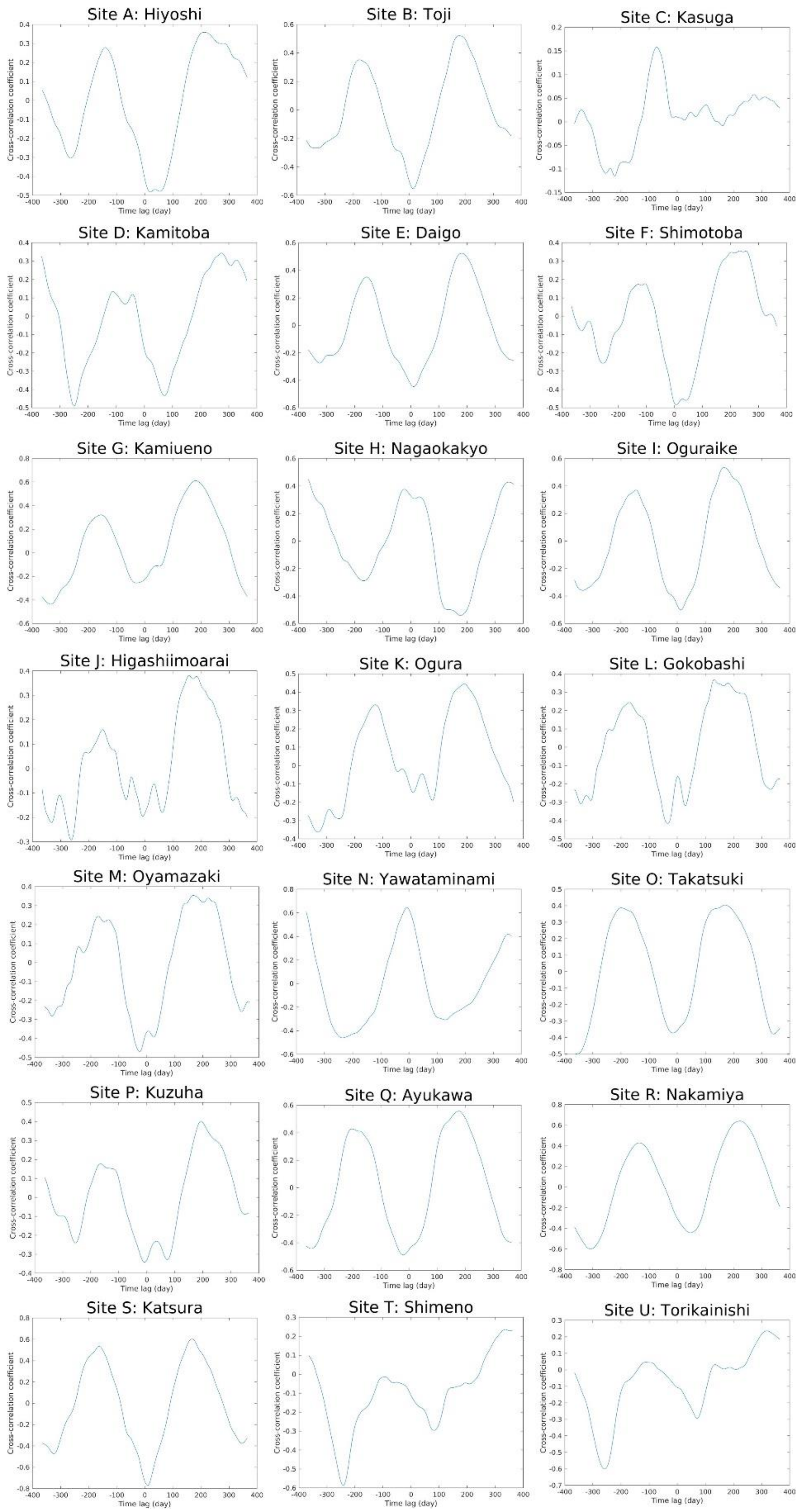

Figure S5. Cross-correlation coefficients between surface displacements and groundwater level changes within a 1-year time lag when $\boldsymbol{adx} = \mathbf{0.25}$ and $\boldsymbol{coh} = \mathbf{0.60}$.

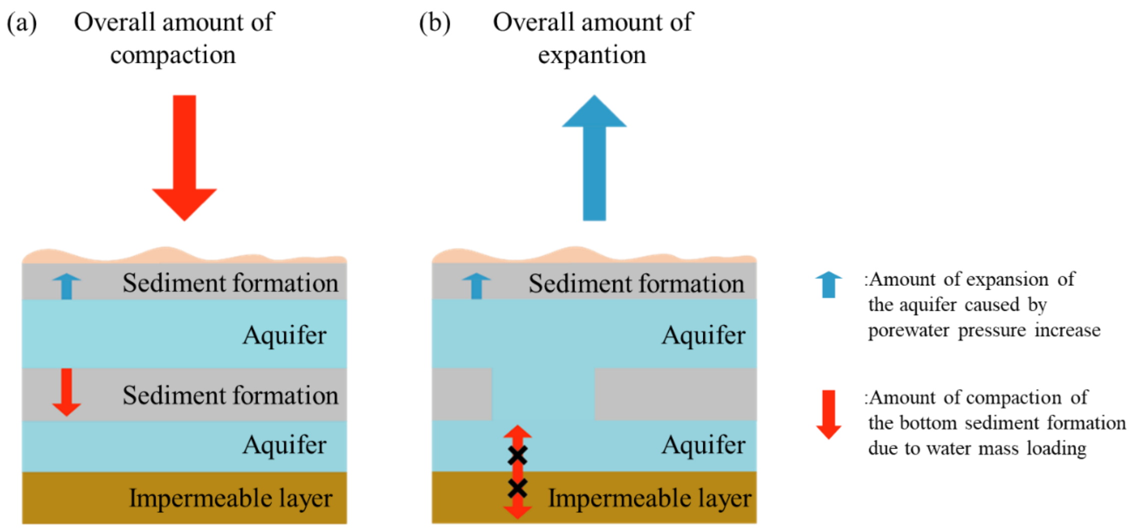

Figure S6. A model of aquifers representing the mechanism of seasonal correlation between surface displacement and groundwater level changes.

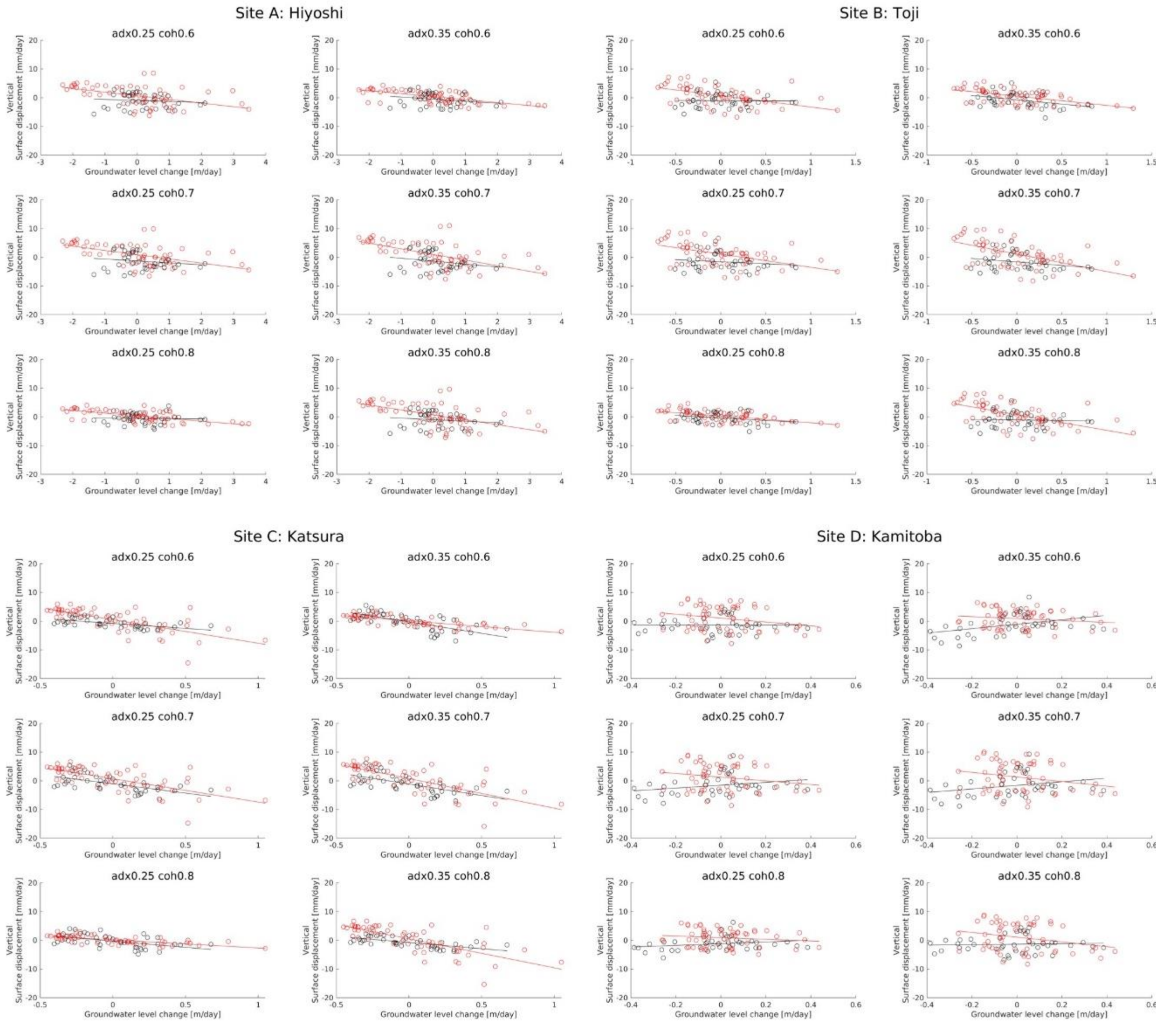

Figure S7. (a) Pseudoelastic constants for all PSInSAR analysis conditions at groundwater level observation sites (A) ~ (D). The black line shows the inverse of the pseudoelastic constants before the earthquake and the red line shows the inverse of the pseudoelastic constants after the earthquake.

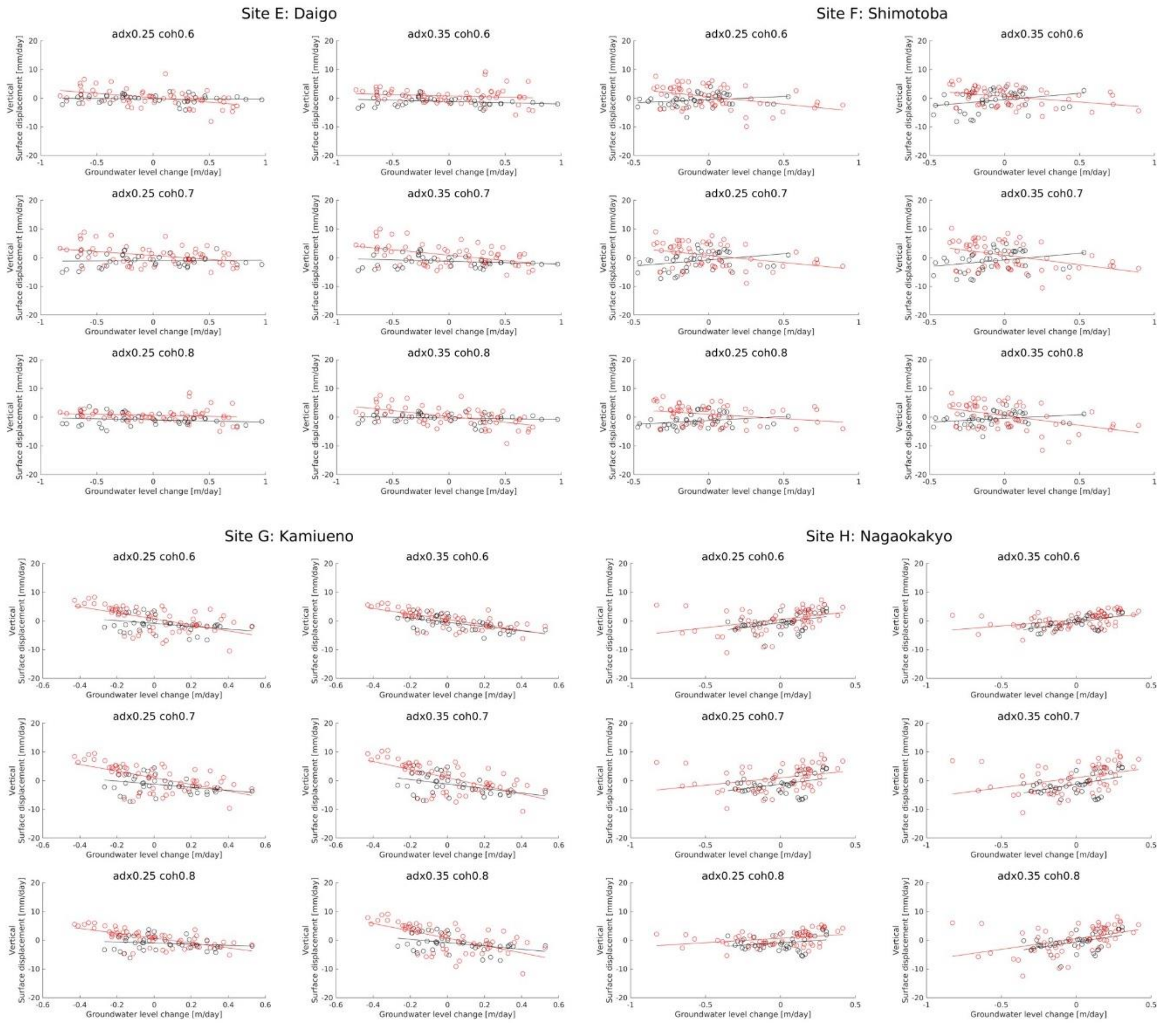

Figure S7. (b) Pseudoelastic constants for all PSInSAR analysis conditions at groundwater level observation sites (E) ~ (H). The black line shows the inverse of the pseudoelastic constants before the earthquake and the red line shows the inverse of the pseudoelastic constants after the earthquake.

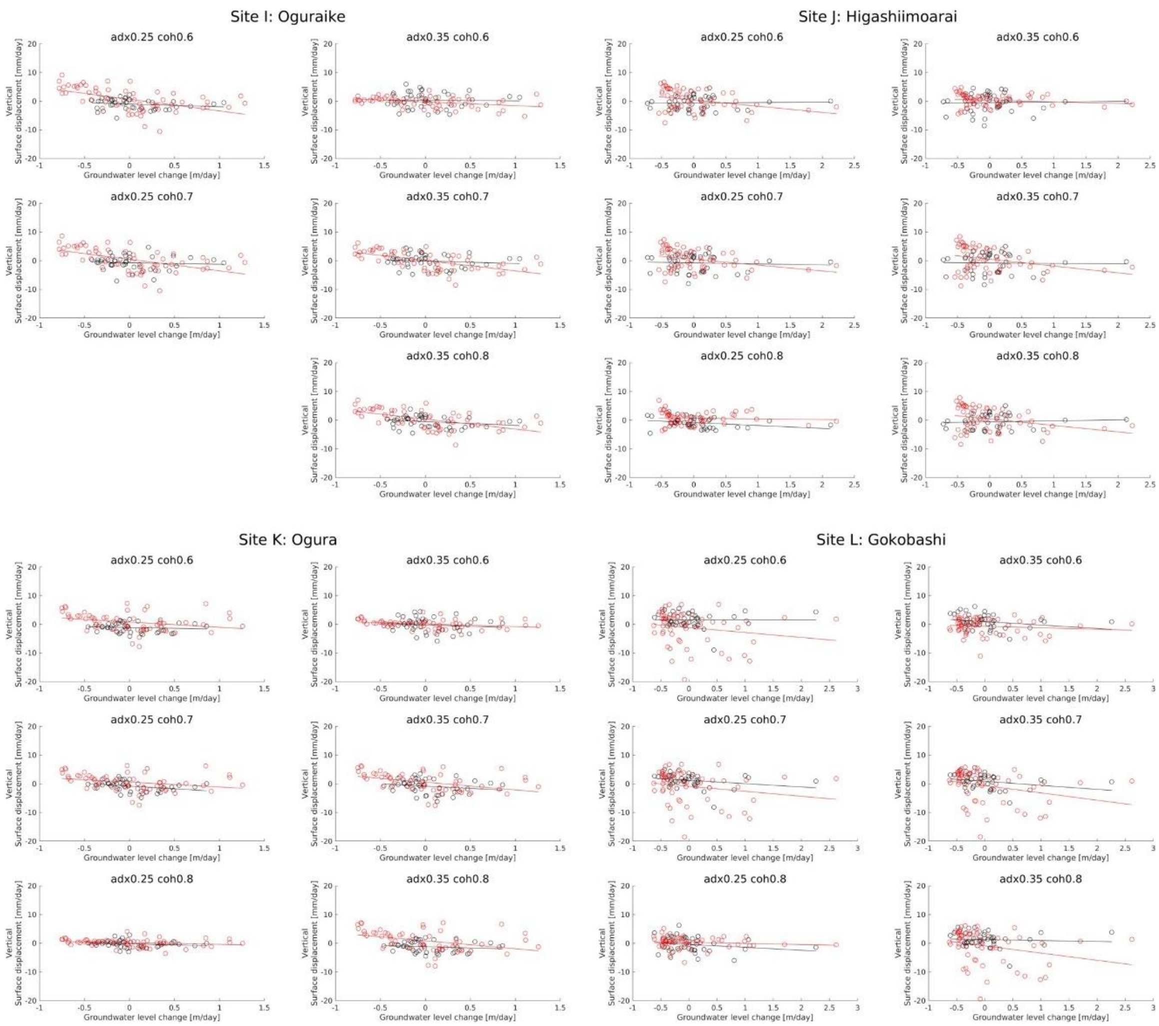

Figure S7. (c) Pseudoelastic constants for all PSInSAR analysis conditions at groundwater level observation sites (I) ~ (L). The black line shows the inverse of the pseudoelastic constants before the earthquake and the red line shows the inverse of the pseudoelastic constants after the earthquake. No PS points were present under $\boldsymbol{adx} = \mathbf{2.5}$, $\boldsymbol{coh} = \mathbf{0.8}$ at Site I: Oguraike.

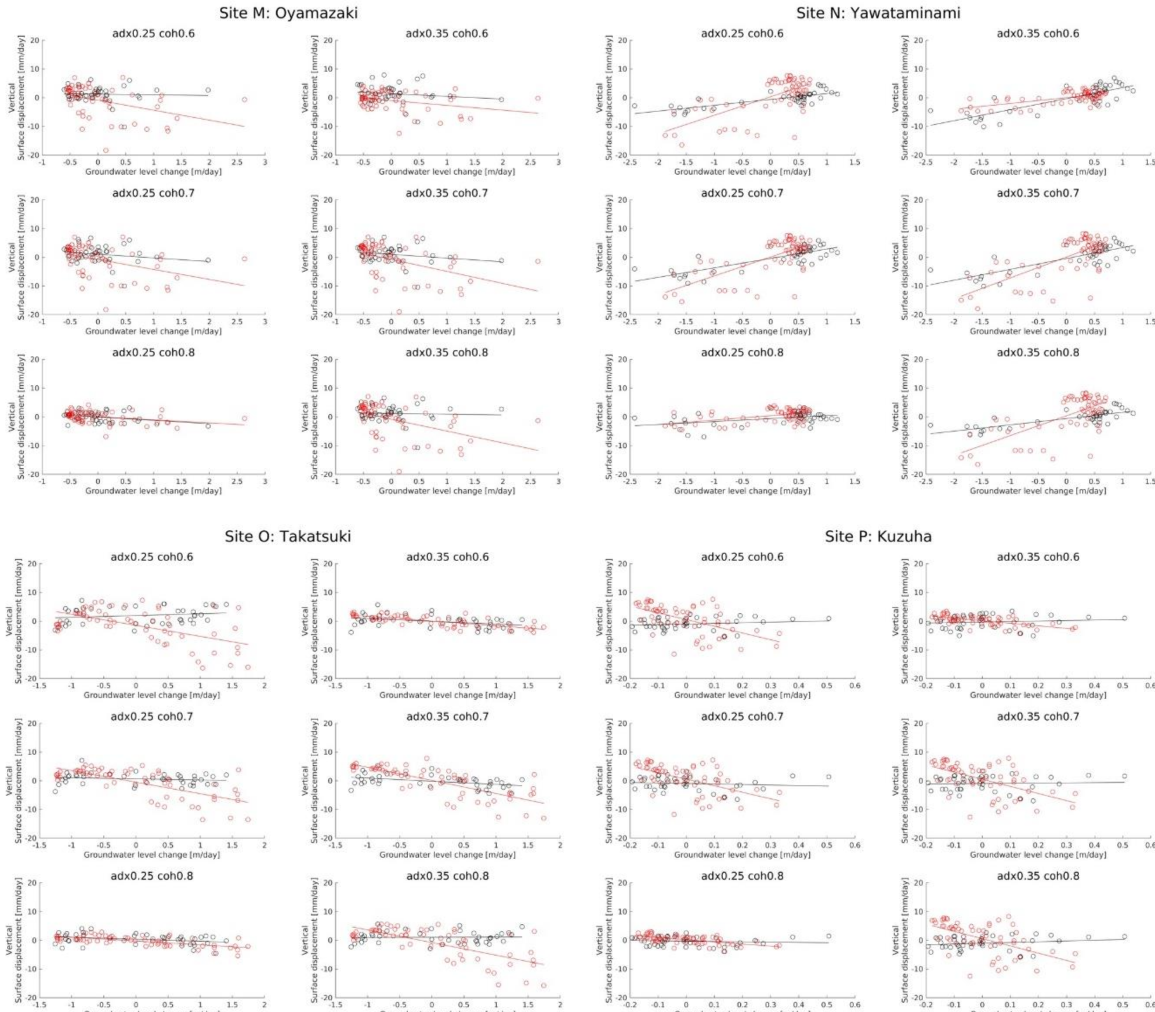

Figure S7. (d) Pseudoelastic constants for all PSInSAR analysis conditions at groundwater level observation sites (M) ~ (P). The black line shows the inverse of the pseudoelastic constants before the earthquake and the red line shows the inverse of the pseudoelastic constants after the earthquake.

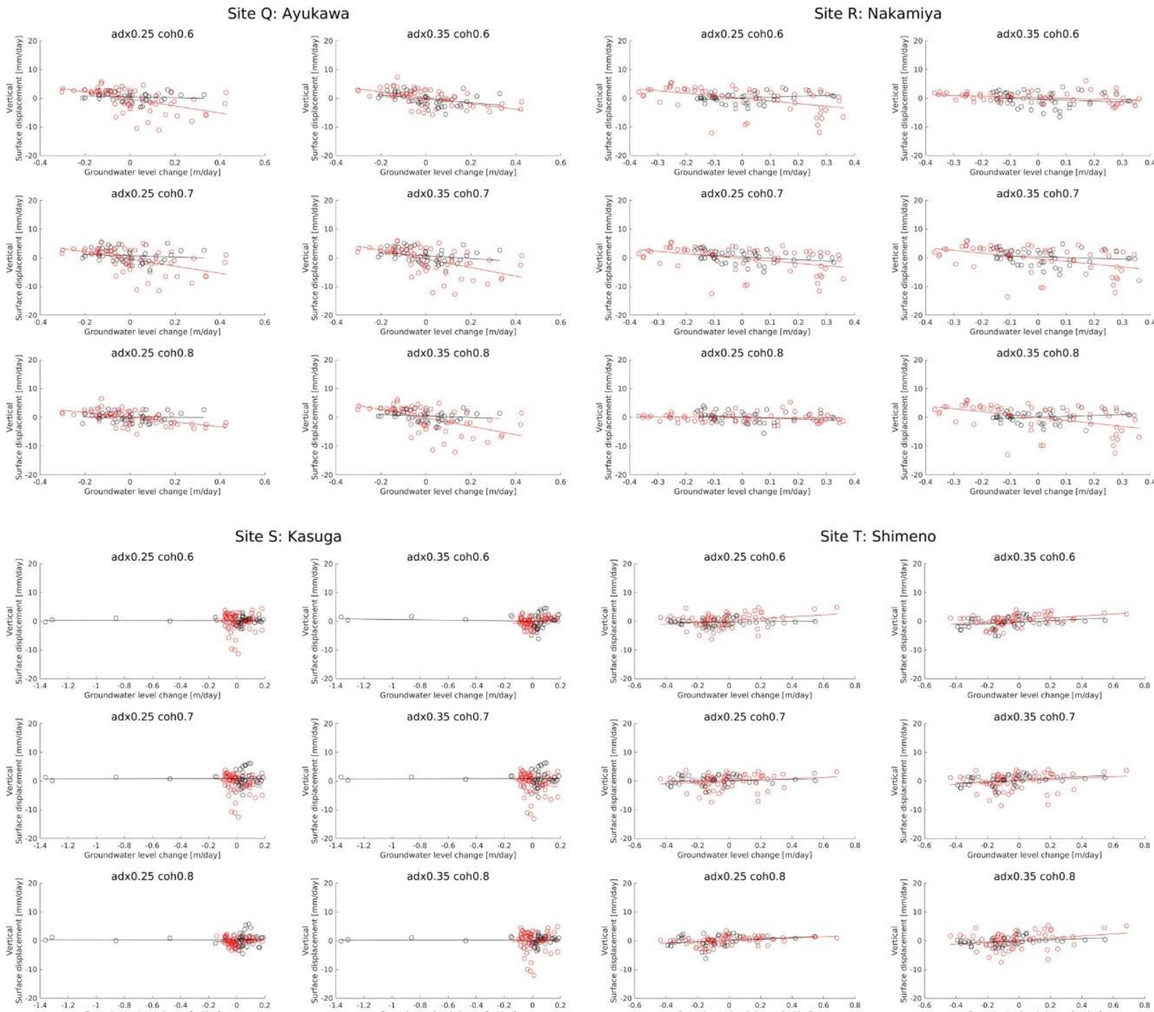

Figure S7. (e) Pseudoelastic constants for all PSInSAR analysis conditions at groundwater level observation sites (Q) ~ (T). The black line shows the inverse of the pseudoelastic constants before the earthquake and the red line shows the inverse of the pseudoelastic constants after the earthquake.

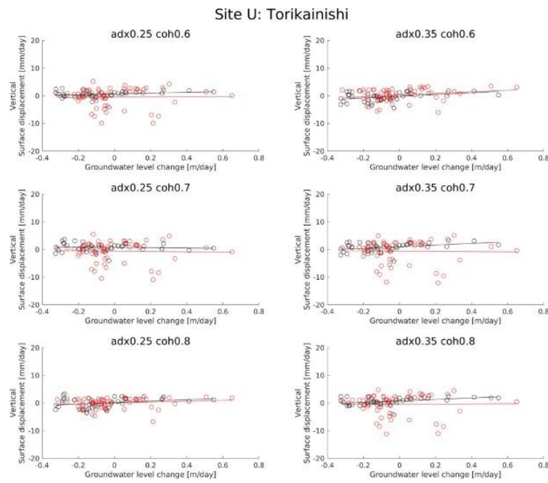

Figure S7. (f) Pseudoelastic constants for all PSInSAR analysis conditions at groundwater level observation sites (U). The black line shows the inverse of the pseudoelastic constants before the earthquake and the red line shows the inverse of the pseudoelastic constants after the earthquake.

Table S1. Data from the European Space Agency's Sentinel-1 satellite used in the PSInSAR analysis are shown.

Satellite	Satellite orbit direction	Data pair observation period	Number of scenes	Incident angle	Satellite traveling direction angle	Path / Frame	Polarization	Beam mode
Sentinel-1	Descending	2016/12/30-2020/12/21	102	37~40°	N13° W	17/474	VV	IW
	Ascending	2016/12/24-2020/12/27	102		N193° S	10/107		

Table S2. The symbol, name, and strainer depth of each groundwater level observation site are shown.

Symbols	Observation site name	Strainer depth (m)			Confined or Unconfined	Latitude (°)	Longitude (°)
		Center	Min	Max			
A	Hiyoshi	8.1	0.0	16.1	U	34.8190722	135.5891667
B	Toji	59.3	53.3	65.3	C	34.9530556	135.8113889
C	Katsura	14.2	8.2	20.2	U	34.8908333	135.6911111
D	Kamitoba	51.7	45.7	57.7	C	34.9027778	135.7336111
E	Daigo	10.2	8.2	12.2	U	34.9888889	135.7677778
F	Shimotoba	43.2	37.2	49.2	C	34.9641667	135.7436111
G	Kamiueno	9.4	6.9	11.9	U	34.9372222	135.7111111
H	Nagaokakyo	45.2	40.2	50.2	C	34.7797222	135.6605556
I	Oguraike	23.3	10.3	36.3	U	34.9761111	135.7041667
J	Higashiimoarai	43.7	37.2	50.2	C	34.8538889	135.6883333
K	Ogura	8.6	5.9	11.2	U	34.9358333	135.6938889
L	Gokobashi	26.0	22.0	30.0	U	34.8163889	135.6600000
M	Oyamazaki	18.3	15.5	21.0	U	34.8991667	135.7833333
N	Yawataminami	20.2	10.7	29.7	U	34.9077778	135.7611111
O	Takatsuki	10.7	7.2	14.2	U	34.8908333	135.6816667
P	Kuzuha	12.0	9.2	14.7	U	34.7727778	135.6008333
Q	Ayukawa	8.2	7.0	9.4	U	34.9386111	135.7433333
R	Nakamiya	10.2	6.2	14.1	U	34.8569444	135.6544444
S	Kasuga	9.5	4.0	15.0	U	34.9877778	135.7525000
T	Shimeno	26.2	22.2	30.2	U	34.7680556	135.5800000
U	Torikainishi	47.5	41.8	53.2	C	34.8600000	135.7150000

Table S3. Average (Ave), standard deviation (Std) of the correlation coefficients in the whole periods for all PSInSAR analysis conditions.

				adx		0.25			0.35	
Symbol	**Name**	**Ave**	**Std**	*coh*	**0.60**	**0.70**	**0.80**	**0.60**	**0.70**	**0.80**
Q	Ayukawa	-0.43	0.03		-0.45	-0.38	-0.40	-0.44	-0.42	-0.47
E	Daigo	-0.39	0.08		-0.43	-0.38	-0.28	-0.32	-0.46	-0.48
L	Gokobashi	-0.19	0.05		-0.16	-0.20	-0.17	-0.11	-0.27	-0.24
J	Higashiimoarai	-0.19	0.04		-0.18	-0.22	-0.19	-0.11	-0.22	-0.18
A	Hiyoshi	-0.43	0.04		-0.41	-0.44	-0.37	-0.40	-0.49	-0.45
D	Kamitoba	-0.04	0.12		-0.18	-0.05	0.09	0.14	-0.06	-0.18
G	Kamiueno	-0.38	0.12		-0.23	-0.34	-0.52	-0.56	-0.39	-0.26
C	Kasuga	0.03	0.03		0.01	0.04	0.08	0.02	0.02	0.01
S	Katsura	-0.70	0.09		-0.73	-0.74	-0.53	-0.65	-0.79	-0.75
P	Kuzuha	-0.34	0.04		-0.33	-0.40	-0.39	-0.28	-0.35	-0.32
H	Nagaokakyo	0.41	0.07		0.33	0.36	0.45	0.54	0.41	0.37
R	Nakamiya	-0.25	0.11		-0.30	-0.36	-0.05	-0.14	-0.34	-0.31
K	Ogura	-0.16	0.06		-0.13	-0.17	-0.08	-0.13	-0.25	-0.22
I	Oguraike	-0.28	0.21		-0.47	-0.45	0.11	-0.09	-0.40	-0.38
M	Oyamazaki	-0.35	0.07		-0.37	-0.39	-0.34	-0.22	-0.42	-0.40
T	Shimeno	-0.06	0.08		-0.11	-0.11	0.12	-0.03	-0.10	-0.10
F	Shimotoba	-0.39	0.09		-0.47	-0.40	-0.26	-0.28	-0.42	-0.48
O	Takatsuki	-0.47	0.05		-0.36	-0.48	-0.49	-0.49	-0.51	-0.50
B	Toji	-0.49	0.05		-0.50	-0.50	-0.41	-0.44	-0.54	-0.54
U	Torikainishi	-0.14	0.07		-0.11	-0.23	-0.03	-0.15	-0.19	-0.10
N	Yawataminami	0.60	0.13		0.63	0.68	0.31	0.63	0.70	0.63

Table S4. Average (Ave), standard deviation (Std), and difference of the correlation coefficients before and after the earthquake for all PSInSAR analysis conditions.

								Before the earthquake						After the earthquake					
		Before the earthquake	After the earthquake		Before the earthquake	After the earthquake	*adx*	0.25			0.35			0.25			0.35		
Symbol	Name	Ave = ①	Ave = ②	② - ①	Std	Std	*coh*	0.60	0.70	0.80	0.60	0.70	0.80	0.60	0.70	0.80	0.60	0.70	0.80
Q	Ayukawa	-0.01	-0.53	-0.52	0.05	0.02		0.00	0.02	0.09	-0.08	-0.04	-0.02	-0.54	-0.49	-0.52	-0.54	-0.51	-0.56
E	Daigo	-0.15	-0.48	-0.32	0.08	0.11		-0.11	-0.01	-0.23	-0.21	-0.19	-0.18	-0.54	-0.50	-0.30	-0.37	-0.56	-0.59
L	Gokobashi	-0.17	-0.19	-0.02	0.09	0.09		-0.03	-0.24	-0.18	-0.29	-0.22	-0.07	-0.19	-0.20	-0.17	-0.02	-0.28	-0.28
J	Higashiimoarai	0.03	-0.26	-0.28	0.16	0.06		0.17	0.03	-0.31	0.03	0.07	0.19	-0.28	-0.30	-0.14	-0.22	-0.31	-0.28
A	Hiyoshi	-0.05	-0.48	-0.44	0.09	0.02		0.03	-0.10	0.08	-0.15	-0.16	0.01	-0.46	-0.49	-0.48	-0.46	-0.53	-0.50
D	Kamitoba	0.40	-0.22	-0.62	0.12	0.09		0.21	0.49	0.42	0.53	0.50	0.25	-0.29	-0.26	-0.08	-0.13	-0.27	-0.30
G	Kamiueno	-0.25	-0.42	-0.17	0.14	0.13		-0.10	-0.25	-0.17	-0.51	-0.35	-0.13	-0.26	-0.37	-0.62	-0.58	-0.41	-0.30
C	Kasuga	-0.05	0.23	0.28	0.02	0.18		-0.05	-0.07	-0.06	-0.08	-0.05	-0.01	0.07	0.23	0.55	0.37	0.14	0.03
S	Katsura	-0.64	-0.74	-0.10	0.06	0.07		-0.64	-0.67	-0.51	-0.69	-0.70	-0.65	-0.77	-0.76	-0.59	-0.71	-0.81	-0.79
P	Kuzuha	0.10	-0.55	-0.64	0.15	0.03		0.27	-0.05	-0.11	0.07	0.13	0.28	-0.53	-0.54	-0.58	-0.58	-0.53	-0.52
H	Nagaokakyo	0.46	0.41	-0.06	0.11	0.07		0.43	0.45	0.29	0.64	0.54	0.44	0.31	0.35	0.49	0.52	0.40	0.36
R	Nakamiya	-0.02	-0.28	-0.26	0.20	0.15		0.26	-0.21	-0.24	-0.13	-0.06	0.24	-0.39	-0.38	0.01	-0.17	-0.39	-0.39
K	Ogura	0.02	-0.21	-0.24	0.15	0.10		0.22	-0.03	-0.24	-0.04	0.02	0.19	-0.22	-0.21	-0.03	-0.19	-0.33	-0.31
I	Oguraike	0.05	-0.37	-0.43	0.13	0.22		0.06	0.05	0.33	-0.07	-0.02	-0.02	-0.55	-0.57	-0.04	-0.10	-0.51	-0.45
M	Oyamazaki	-0.21	-0.39	-0.18	0.08	0.09		-0.12	-0.25	-0.32	-0.25	-0.23	-0.11	-0.43	-0.43	-0.35	-0.21	-0.47	-0.46
T	Shimeno	-0.01	-0.07	-0.06	0.15	0.07		-0.22	-0.12	0.23	0.13	0.00	-0.09	-0.09	-0.11	0.07	-0.08	-0.13	-0.10
F	Shimotoba	0.14	-0.55	-0.68	0.17	0.04		-0.07	0.15	0.43	0.23	0.14	-0.06	-0.57	-0.57	-0.46	-0.53	-0.58	-0.58
O	Takatsuki	-0.04	-0.63	-0.58	0.14	0.06		0.15	0.02	-0.22	-0.21	-0.05	0.07	-0.51	-0.64	-0.64	-0.62	-0.67	-0.68
B	Toji	-0.23	-0.55	-0.32	0.10	0.06		-0.07	-0.25	-0.25	-0.35	-0.32	-0.12	-0.57	-0.55	-0.47	-0.48	-0.59	-0.61
U	Torikainishi	-0.07	-0.16	-0.09	0.13	0.06		-0.13	-0.29	0.14	0.00	-0.09	-0.05	-0.11	-0.22	-0.09	-0.21	-0.23	-0.12
N	Yawataminami	0.71	0.58	-0.12	0.19	0.14		0.75	0.83	0.30	0.77	0.83	0.75	0.67	0.67	0.32	0.46	0.69	0.68